Arecibo Radar Astrometry of the Galilean Satellites from 1999 to 2016

Item Type	Article
Authors	Brozović, Marina; Nolan, Michael C.; Magri, Christopher; Folkner, William M.; Jacobson, Robert A.; Harcke, Leif J.; McMichael, Joseph G.; Richardson, James E.; Harmon, John K.; Taylor, Patrick A.; Benner, Lance A. M.; Giorgini, Jon D.; Ostro, Steven J.; Perillat, Philip J.; Hine, Alice A.; Naidu, Shantanu P.; Slade, Martin A.; Rożek, Agata; Rodriguez-Ford, Linda A.; Zambrano-Marin, Luisa F.
Citation	
DOI	
Publisher	IOP PUBLISHING LTD
Journal	ASTRONOMICAL JOURNAL
Rights	
Download date	27/08/2022 20:32:36
Item License	
Version	Final published version
Link to Item	http://hdl.handle.net/10150/641020

Arecibo Radar Astrometry of the Galilean Satellites from 1999 to 2016

Marina Brozović[1], Michael C. Nolan[2], Christopher Magri[3], William M. Folkner[1], Robert A. Jacobson[1] , Leif J. Harcke[1],
Joseph G. McMichael[1], James E. Richardson[4], John K. Harmon[5], Patrick A. Taylor[5,6,7], Lance A. M. Benner[1], Jon D. Giorgini[1],
Steven J. Ostro[1], Philip J. Perillat[5,6], Alice A. Hine[5], Shantanu P. Naidu[1] , Martin A. Slade[1], Agata Rożek[8],
Linda A. Rodriguez-Ford[5,6], and Luisa F. Zambrano-Marin[5,6]

[1] Jet Propulsion Laboratory, California Institute of Technology, Pasadena, CA 91109-8099, USA; Marina.Brozovic@jpl.nasa.gov
[2] Lunar and Planetary Laboratory, The University of Arizona, Tucson, AZ 85721, USA
[3] University of Maine at Farmington, Farmington, ME 04938, USA
[4] Planetary Science Institute, 1700 E. Fort Lowell Road, AZ 85719, USA
[5] Arecibo Observatory, Arecibo, PR 00612, USA
[6] Universities Space Research Association, Columbia, MD 21046, USA
[7] Lunar and Planetary Institute, Houston, TX 77058, USA
[8] Centre for Astrophysics and Planetary Science, The University of Kent, Canterbury CT2 7NH, UK
Received 2019 December 6; revised 2020 January 13; accepted 2020 January 15; published 2020 March 10

Abstract

Harmon et al. Arecibo radar observations from 1992 provided some of the most precise line-of-sight distance (ranging) measurements of Ganymede and Callisto to date. We report 18 new ranges obtained at Arecibo from 1999 to 2016, among which are the first measurements of Io and Europa. We also report accompanying line-of-sight velocity (Doppler frequency) measurements. In 2015, we detected Europa, Ganymede, and Callisto with time-delay (range) resolutions as fine as 10 μs (1.5 km) while Io was detected with 70 μs (10.5 km) resolution. We estimated residuals for the radar measurements with respect to the latest JPL satellite ephemeris JUP310 and planetary ephemeris DE438. We found that the rms of the time-delay residuals are 29 μs for Io, 21 μs for Europa, 58 μs for Ganymede, and 275 μs for Callisto. When normalized by the measurement uncertainties, these correspond to the rms of 0.82, 1.25, 2.17, and 3.17 respectively. As such, the orbit of Callisto has the largest residuals and may benefit from an orbital update that will use radar astrometry. All Doppler residuals were small and consistent with their 1σ uncertainties.

Unified Astronomy Thesaurus concepts: Astrometry (80); Radar astronomy (1329); Galilean satellites (627)

1. Introduction

Io, Europa, Ganymede, and Callisto are the Galilean moons of Jupiter, ranging in diameter from $\sim$3600 to 5300 km. They revolve around the planet in equatorial, near-circular orbits, with semimajor axes of 0.42, 0.67, 1.07, and 1.88×10^6 km respectively. The orbits of Io, Europa, and Ganymede are in a Laplace resonance defined by the resonant argument $\dot{\lambda}_{Io} - 3\dot{\lambda}_{Europa} + 2\dot{\lambda}_{Ganymede} = 0$ where $\dot{\lambda}$ refers to the mean longitude rate. A consequence of this resonance is that these three moons never align in a triple conjunction. Their orbital dynamics provides a window into the Jupiter system's formation and tidal evolution (Lainey et al. 2009; Lainey 2016).

Astrometric observations are used for orbital determination of all solar system bodies. Long data arcs and high-precision astrometry are a prerequisite for high-fidelity orbital fits. Measurements of the Galilean moons have a long history. Sampson (1921) and Lieske (1978) used eclipse observations (Lieske 1986a, 1986b) in the development of the first ephemerides. Lieske (1980, 1998) added astrometric observations of mutual events (eclipses and occultations between two moons). Optical astrometry is usually reported in the form of relative positions between two satellites or between Jupiter and a satellite, but some high-precision absolute positions of satellites are referenced directly to the stellar background (Stone 2000, 2001; Stone & Harris 2000). In recent years Galilean satellite ephemeris development included ground-based optical data, *Voyager* and *Galileo* spacecraft imaging data, range and Doppler tracking of *Voyager* 2, and Doppler tracking of *Galileo* during close satellite flybys (Campbell et al. 1983;

Jacobson et al. 2000). Observations from the Juno spacecraft have not yet been included.

Historically, the most precise ground-based measurements of the positions of the Galilean satellites, $\sim$25 mas (milliarcseconds) on the plane of sky, originated from mutual events (Lainey et al. 2009). The season of mutual events at Jupiter occurs every six years when the planet passes though the equinox. Morgado et al. (2019b) reported on even more precise measurement based on the first recorded stellar occultation of Europa on 2017 March 31. They estimated the position of Europa with 0.8 mas uncertainty. At Jovian distances, $1''$ is $\sim$3000 km, which means that the stellar occultation had $\sim$2.4 km uncertainty. This exceptionally precise measurement is only surpassed by the *Voyager* 2 spacecraft ranges that had a precision of about a few hundred meters. Unfortunately, serendipitous stellar occultations of the Galilean moons do not occur often because Jupiter needs to be in a region of sky with a dense star field. Such opportunities occur in 2019, 2020, and 2031 (Gomes-Júnior et al. 2016; Morgado et al. 2019b).

Harmon et al. (1994) reported on the first radar ranging measurements of Ganymede and Callisto from Arecibo in 1992. They obtained two measurements of Ganymede with 3 and 7 km precision and two measurements of Callisto with 14 km precision. This was before Arecibo's S-band radar upgrade in 1999 after which the system gained more than an order of magnitude in sensitivity. The work presented here reports more radar astrometry obtained at Arecibo from 1999 to 2016. To date, radar measurements have not been used to update

the Galilean satellites ephemeris, but we expect to do so in the future.

2. Methods

2.1. Delay-Doppler Imaging

Planetary radar transmits a circularly polarized waveform of a fixed frequency. The signal is transmitted for the duration of the round-trip-time (RTT) to the target and an echo is received for the same duration (unless the target sets before the cycle is complete). The signal reflects off the target in the same sense of circular polarization (SC) as the transmitted signal and in the opposite sense (OC). Echoes from a surface that is smooth at radar wavelengths (decimeter scales) will return almost entirely in the OC polarization. The SC echoes can result from multiple scattering from rough surfaces, single scattering from surfaces with radii of curvature comparable to the radar wavelength, and from coherent volume backscattering. Europa, Ganymede, and Callisto have stronger SC echoes and Io has a stronger OC echo (Campbell et al. 1977, 1978; Ostro et al. 1992). Ostro et al. (1992) interpreted SC/OC > 1 for Europa, Ganymede, and Callisto as "the satellite regolith looks to the radar like a disordered random medium containing anisotropic scatterers." In general, the echo strength depends on size, rotation rate, radar albedo, and subradar latitude as well as on the radar system parameters (see Ostro 1993 for details).

Delay-Doppler imaging is a standard radar technique in which the echo from a target is mapped from 3D spatial coordinates into time-delay and Doppler frequency 2D coordinates (Ostro 1993; Black 2002). Radar transmits a circularly polarized signal that is modulated in time either with a code that switches the phase of a sinusoidal wave by 180° or with a linear frequency modulation (chirp). Arecibo delay-Doppler imaging utilizes the first technique. Here, the transmitted signal is continuous, but binary phase-shift keying is applied with a code repetition period, CRP = Lb. Here, $L = 2^n$-1 is the length of a pseudo-noise maximal-length shift-register sequence, b is the phase flip interval or time baud, and n is an integer that determines the code length. We refer to this technique here as "repeating code" or "binary phase coding." Repeating code is widely used for observations of near-Earth asteroids and comets, but radar observations of planets and planetary satellites often use different coding we call the "long code" method (Harmon 2002). The fundamental difference between the long code and the repeating code is that the long code has a pseudo-random phase modulation of the outgoing signal that, for all practical purposes, does not repeat within an observation. Consequently, there is no delay folding of the echo as would be the case with the standard code, and the self-clutter from the long-code decoding process only appears as additive random noise. In principle, the code does repeat after $(2^{40}-1)b$, but that is longer than distances within the solar system. The long code is used for radar imaging of large, or rapidly rotating targets such as Mercury, Venus, Mars, the Galilean satellites, and some main belt asteroids where the product of the Doppler bandwidth and the delay depth of the target is >1. The long code method was developed for ionospheric observations at Arecibo (Sulzer 1986), and was first tested on Mars in 1990 (Harmon 2002).

At the receiving end, the signal is quadrature mixed to baseband, passed through a matched filter and recorded in the form of digitized voltages. A high-speed data acquisition system is used to make measurements of the received signal
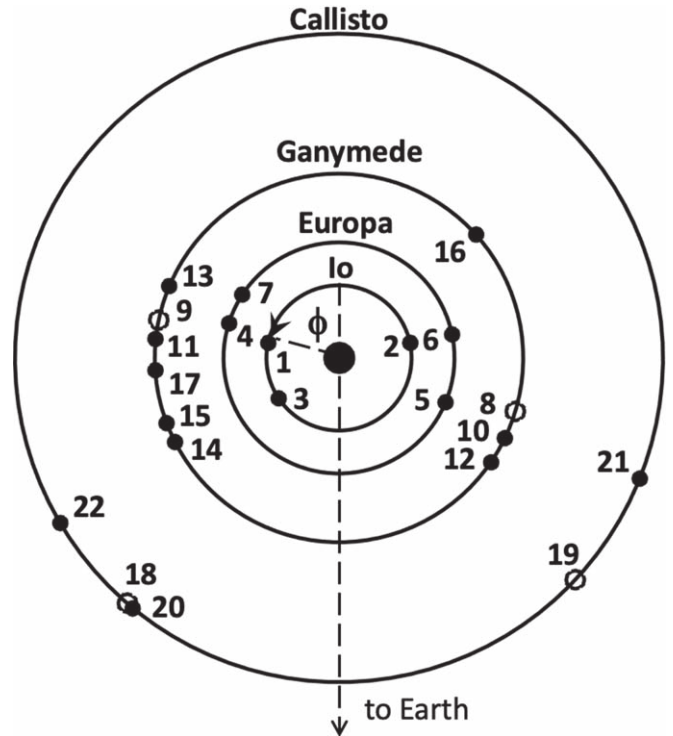
Figure 1. Orbital geometry of the observations. Angle ϕ denotes the geocentric orbital phase as defined in Harmon et al. (1994). The phase is measured from the Earth–Jupiter line in the counterclockwise direction. The numbers refer to the observation times in Table 1. The empty circles denote observations from Harmon et al. (1994).

in real time. The signal is sometimes sampled two to four times per baud resulting in time-delay (range) pixel resolution of baud/(samples per baud) μs. More details can be found in Magri et al. (2007). Imaging with multiple samples per baud improves the signal-to-noise-ratios (S/Ns), but adjacent pixels are correlated, and the effective range resolution still remains roughly equal to the baud.

Radar observations use the target's ephemeris to tune either the transmitter's or the receiver's programmable oscillator to the changing Doppler frequencies due to relative motions of the target and the observer. For delay-Doppler imaging, one also adjusts the sampling time base according to the ephemeris-estimated rate of change of time delay. This keeps the received radar echo at a fixed position. We used the Yeomans et al. (1992) method to calculate radar observables for 1999–2016 experiments. The predicts tabulated the time delays and Doppler shifts from the observatory to the subradar point of the International Astronomical Union (IAU) reference ellipsoid for a target satellite. We obtained absolute radar measurements of the satellite's line-of-sight position and velocity by adding offsets between the observed and the predicted values. This radar astrometry is suitable for use in an orbital update.

2.2. Observations

Figure 1 shows geometry of the radar observations including the Harmon et al. (1994) observations of Ganymede and Callisto. Table 1 lists details about observational setups and geometries. Each satellite was imaged multiple times at both eastern and western elongations. Jupiter is a strong S-band radio source, so observations of the Galileans are always

Table 1
Masterlog of Arecibo Radar Observations of the Galilean Satellites

Num.	Date	Time START hh:mm:ss	(UTC) STOP hh:mm:ss	Baud (μs)	spb	R.A. (°)	Decl. (°)	Distance (au)	Ob-lon (°)	Ob-lat (°)	ϕ (°)	Sol	Ptx (kW)
	Io												
1	2015 Feb 12	04:14:15	05:26:31	70	2	139.7	16.7	4.352	78.3	−0.2	77.9	jup310	855
2	2015 Feb 13	04:09:49	05:22:07	70	2	139.5	16.7	4.354	281.4	−0.2	281.7	jup310	900
3	2015 Feb 14	04:05:19	05:17:37	70	2	139.4	16.8	4.354	124.3	−0.2	124.1	jup310	900
	Europa												
4	1999 Nov 8	03:01:06	04:07:37	100	2	26.5	9.3	4.006	74.2	3.0	72.5	1555.comb	465
5	2015 Feb 8	04:31:32	05:43:41	10	2	140.1	16.5	4.345	250.0	0.2	247.4	jup310	853
6	2016 Jan 19	08:35:34	09:05:41[a]	70	2	174.1	4.0	4.787	284.2	−1.9	281.6	jup310	675
7	2016 Jan 31	07:43:18	08:18:00[a]	20	4	173.6	4.3	4.647	57.8	−1.9	56.7	jup310	606
	Ganymede												
8	1992 Feb 20	05:20:20	06:33:41[h]	100	1	162.8	8.8	4.422	255.5	−1.3	253.2	E-3	420
9	1992 Mar 9	04:00:40	05:14:09[h]	100	1	160.8	9.6	4.426	80.6	−1.2	78.2	E-3	420
10	1999 Oct 30	03:58:19	04:58:00[a]	40	2	27.5	9.7	3.969	246.6	3.1	244.1	1556.comb	463
11	1999 Nov 3	03:42:05	04:05:17[a]	100	2	27.2	9.6	3.984	87.0	3.1	84.7	1556.comb	475
12	1999 Nov 6	03:08:44	04:15:00	100	2	26.6	9.4	3.991	238.1	3.1	235.6	1556.comb	474
13	2015 Jan 31	05:16:10	06:28:29	70	2	141.3	16.2	4.355	69.7	−0.1	67.1	jup310	830
14	2015 Feb 1	05:03:06	06:15:17	10	2	141.2	16.2	4.347	119.7	−0.1	117.1	jup310	877
15	2016 Jan 18	08:40:34	09:09:50[a]	70	2	174.2	3.9	4.797	113.2	−1.8	110.7	jup310	677
16	2016 Jan 22	08:23:04	08:53:52[a]	40	2	174.0	4.1	4.753	314.2	−1.8	311.9	jup310	833
17	2016 Feb 1	07:39:10	08:14:00[a]	20	4	173.6	4.3	4.634	96.5	−1.8	93.9	jup310	685
	Callisto												
18	1992 Mar 3	04:28:30	05:41:35[h]	100	1	161.6	9.3	5.394	138.9	−1.4	139.2	E-3	420
19	1992 Mar 7	04:09:20	05:22:27[h]	100	1	160.9	9.6	5.395	225.6	−1.4	226.9	E-3	420
20	2000 Dec 6	03:55:20	05:02:38	500	2	63.4	20.3	4.054	140.1	2.9	140.5	1642.comb	895
21	2000 Dec 11	03:02:34	04:10:16	500	2	62.4	20.1	4.078	248.1	2.9	248.2	1642.comb	914
22	2015 Feb 7	04:49:26	06:01:30	10	2	140.5	16.4	4.340	120.5	−0.3	120.6	jup310	852

Note. Radar observations were conducted monostatically at S-band (2380 MHz, 12.6 cm). The first column lists the observation numbers to which we refer to in Figure 1. The times refer to the start and the end of reception on each day. Most of our reception times are equal to one full RTT except for the observations marked with the letter *a*. These had shorter reception times either because Jupiter was setting, or because another observing target was on the schedule. We list the baud (time-delay resolution in μs) and number of samples per baud (spb) for the long code setups. The time-delay resolution of a pixel is baud/spb. We also list the parameters associated with the observing geometry: R.A., decl., distance (in au), observer (subradar) west longitude and latitude in the middle of the reception time, and the geocentric orbital phase ϕ as defined in Figure 1. The last two columns list the orbital solution (Sol) used to compute the delay-Doppler predicts for the subradar point of each satellite and the transmit power. We include the data points from Harmon et al. (1994), marked with the letter *h*, for completeness. The data were obtained before the Arecibo's S-band system underwent an upgrade which increased the sensitivity by about a factor of 20.

Table 2
Physical Properties of the Galilean Satellites

	Radius (km)	Rotation Rate (deg day⁻¹)	Spin pole		Max. Doppler bw in S-band (Hz)	Max. visible extent (μs)	Max. S-band S/Ns/RTT
			α_0 (deg)	δ_0 (deg)			
Io	1829.4 × 1819.4 × 1815.7	203.48895	268.05	64.50	2396	12196	180
Europa	1562.6 × 1560.3 × 1559.5	101.37472	268.08	64.51	1020	10417	1500
Ganymede	2631.2 ± 1.7	50.31761	268.20	64.57	852	17541	2600
Callisto	2410.3 ± 1.5	21.57107	268.72	64.83	335	16069	1600

Note. Listed are the radii, rotation rates, and the spin poles for the Galilean satellites according to the latest International Astronomical Union report and the references within (Archinal et al. 2018). The original references for the sizes and shapes are Io—Thomas et al. (1998b); Europa—Nimmo et al. (2007); Ganymede—Anderson et al. (2001a); and Callisto—Anderson et al. (2001b). Thomas et al. (1998b) quoted 0.3 km error based on the differences between the best ellipsoidal fit and the best hydrostatic equilibrium fit. Nimmo et al. (2007) estimated a mean radius error of 0.3 km and $a–c = 3.0 ± 0.9$ km, where a and c are the long and short axes. We list the leading terms for the International Celestial Reference Frame spin pole at the epoch J2000.0. The maximum Doppler bandwidth in S-band, B, was calculated from $B = (4\pi D \cos\delta)/\lambda P$, where D is the diameter, δ is the radar sublatitude, λ is the transmitter wavelength, and P is the rotation period (Ostro 1993). The maximum visible extent was calculated from the equatorial radius converted to μs. The S-band S/Ns were calculated based on Equation (2) in Ostro (1993). The S/Ns depend on Arecibo's system parameters, the satellite's physical parameters, and the time of integration. The maximum S-band S/Ns were calculated assuming Jupiter in opposition at 4.35 au, a transmitter power of 900 kW, a system temperature of 23 K, and a gain of 10 K Jy⁻¹. The SC radar albedos for Europa, Ganymede, and Callisto were assumed to be 1.58, 0.82, and 0.37, respectively (Ostro et al. 1992). The OC albedo for Io was assumed to be 0.2 (Ostro 1993).
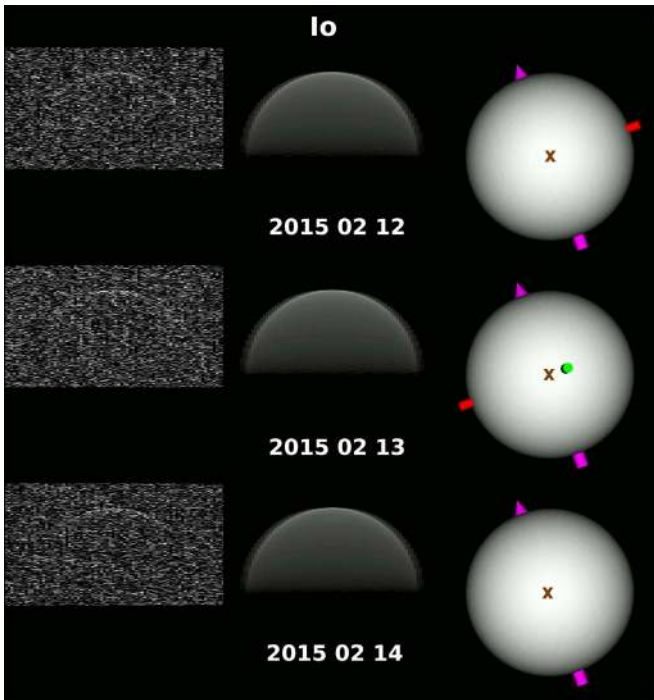
Figure 2. Collage of, from left to right, delay-Doppler OC+SC radar images, fits, and the *Shape* software plane-of-sky renderings of the shape model for Io (Table 2). In the data and fits, time-delay increases from top to bottom, and Doppler frequency increases from left to right. The image resolutions, dimensions, and observing midtimes are listed in Table 3. Plane-of-sky view is contained in a 4700.0 × 4700.0 km square with 4701 × 4701 pixels. The magenta arrow shows the orientation of the spin vector, while the red and green shafts, visible in the second row, denote the long and intermediate axis. The "X" marks the subradar point.

scheduled near the maximum plane-of-sky angular separation from the planet.

Ganymede and Callisto were first imaged in 1992 with 100 μs (15 km) range resolution. Europa was first imaged in 1999 with 100 μs (15 km) range resolution while the newly upgraded *S*-band system at Arecibo was still at half power (Harmon 2002). Harcke et al. (2001) reported on observations of Europa, Ganymede, and Callisto from 2000 with 250–500 μs (37.5–75 km) range resolutions. These images were taken for the purpose of obtaining reflectance maps, and the published data did not initially contain the loopback information needed to measure the time-delay and Doppler offsets from the ephemerides used in the experiment. We located both the published and unpublished 1999 and 2000 data in Arecibo's data repository, and they were reprocessed to include astrometric calibration so that they become suitable for astrometric measurements. Table 1 lists six reprocessed delay-Doppler observations from 1999 and 2000: one of Europa, three of Ganymede, and two of Callisto, varying in resolutions from 40 to 500 μs (6–75 km).

We organized an extensive observing campaign in 2015 and 2016 with the goal of obtaining the most precise ranging measurements to date (Table 1). Our objective was to resolve the location of the subradar point at the center of the leading edge of an echo as opposed to image the entire satellite. The echo power is the strongest at the subradar point, so it is straightforward to detect even with high-resolution bauds.

We obtained 12 delay-Doppler images with resolutions between 10 and 70 μs (1.5–10.5 km). Europa, Ganymede, and Callisto were imaged with 1.5 km range resolution, which is comparable with the radii uncertainties reported by Nimmo et al. (2007) and Anderson et al. (2001a, 2001b). We found Io to be the most difficult to observe due to its low radar albedo (compared to the other satellites), which significantly reduces the S/Ns (Table 2). Imaging of Io requires that Arecibo transmits at full power (900 kW), that Jupiter is close to opposition, and that Io is near maximum elongation. Furthermore, Arecibo's observing window needs to overlap with the maximum elongation time. Arecibo can achieve at most one full transmit and receive cycle during an observing session. If the target sets before the receiving cycle is complete, the S/Ns are reduced. In 2015, we had favorable conditions to obtain three delay-Doppler images of Io with 70 μs (10.5 km) resolution (Figure 2).

Figures 3–5 show delay-Doppler images of Europa, Ganymede, and Callisto. There is a clear difference between the echoes obtained with coarser bauds and those taken with high-resolution bauds. As expected, the high-resolution images show only the leading edge, while the coarse-resolution images of Ganymede from 1999 and 2015 and Callisto from 2000 clearly show radar-bright features well behind the leading edge.

2.3. Astrometric Measurements

Harmon et al. (1994) showed that radar measurements of the line-of-sight distances and velocities of the Galilean satellites can be very precise. We followed the procedure described in Harmon et al. to measure the location of each satellite's subradar point in range and Doppler frequency. The general idea is to construct a template radar echo that gets shifted in time-delay and frequency until it aligns with the observed data. The measured shifts represent corrections to the ephemerides used in experiments and the resulting absolute values can be used to improve the orbits.

The synthetic radar echo was constructed by convolving the radar ambiguity function $\psi^2(\tau, f)$ and target scattering function $\sigma(\tau, f)$. Here, τ is the time-delay and f is the Doppler frequency. The functions are defined as:

$$\psi^2(\tau, f) = (1 - |\tau|/b)^2 \left(\frac{\sin(\pi f/f_r)}{\pi f/f_r} \right)^2 \qquad (|\tau| \leqslant b) \qquad (1)$$

$$\sigma(\tau, f) = (1 - \tau/\tau_0)^q [1 - (f/f_0)^2 - (1 - \tau/\tau_0)^2]^{-1/2}. \quad (2)$$

Here, b is the baud of the synthetic radar echo, f_r is the frequency resolution of the synthetic radar echo, τ_0 is the visible extent of the satellite in time-delay, and f_0 is the center-to-limb Doppler bandwidth of the echo. Exponent q is related to the radar scattering function, taken to be $\sigma_0 (\theta) \propto \cos^q \theta$, where θ is the scattering angle. We used $q = 1.5$ for Europa, Ganymede, and Callisto (Ostro et al. 1992; Harmon et al. 1994; Black et al. 2001). There are no published values of q for Io, but Ostro (1993) noted that estimated q values for most surfaces fall between one and two. The lower bound corresponds to a geometric scattering law and the upper bound corresponds to pure Lambert scattering law. We adopted Lambert scattering law to model the synthetic echo of Io.

Harmon et al. (1994) constructed synthetic echoes that had higher resolutions than the radar data. They oversampled the 100 μs, 10 Hz delay-Doppler images of Ganymede and Callisto by a factor of 10 in time-delay and by a factor of 5 in Doppler frequency, and constructed the corresponding synthetic echoes as
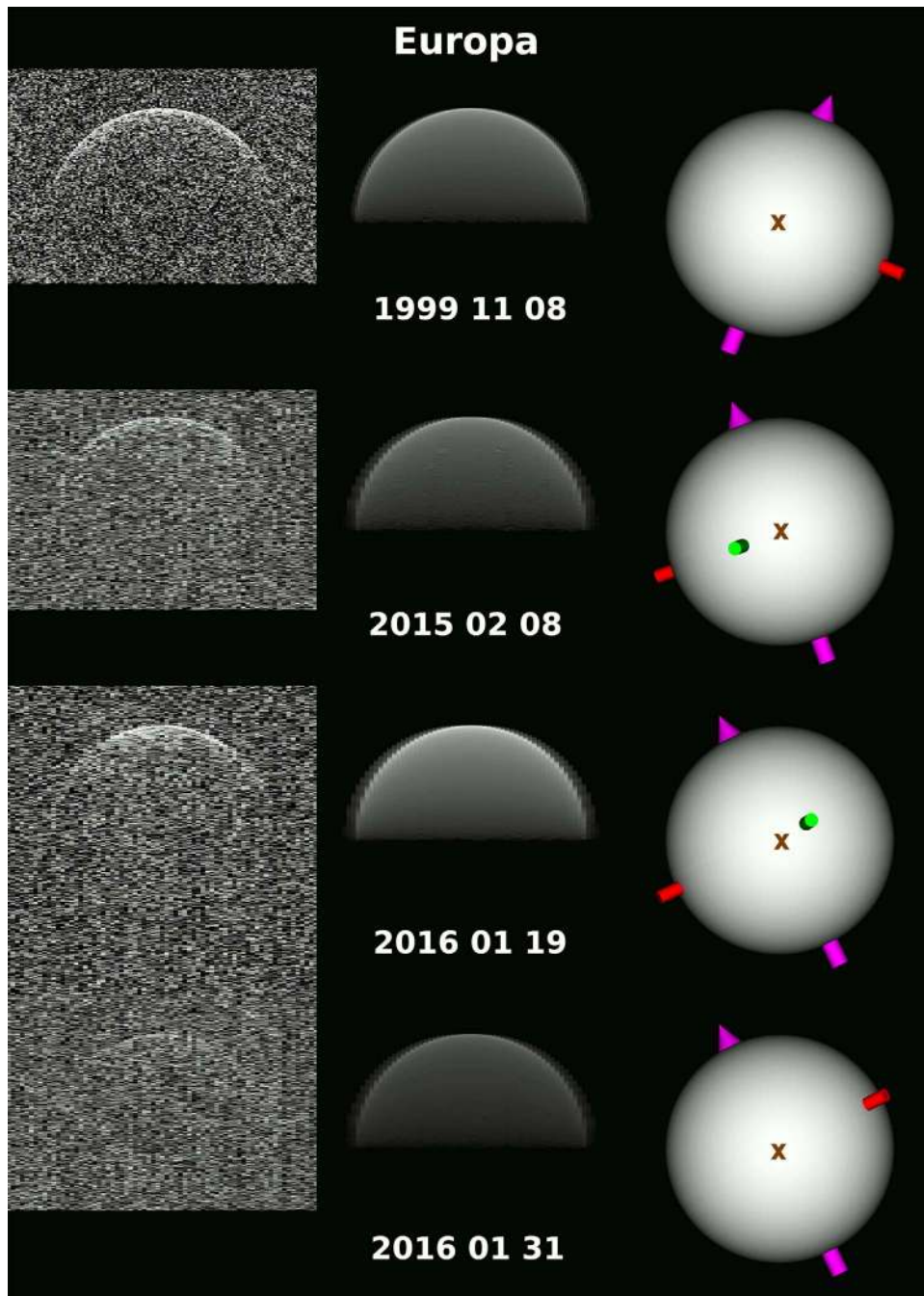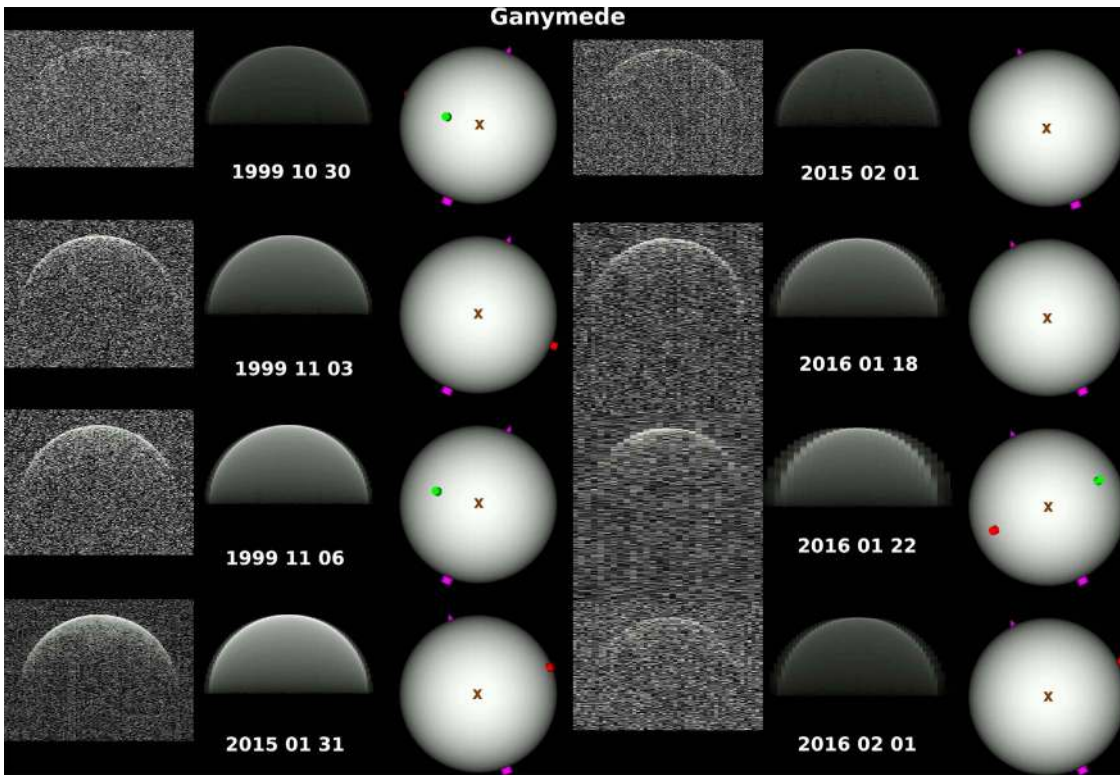
Figure 3. Collage of, from left to right, delay-Doppler SC radar images, fits, and the *Shape* software plane-of-sky renderings of the shape model for Europa (Table 2). Plane-of-sky view is contained in a 4200.0 × 4200.0 km square with 4201 × 4201 pixels. The rest of the caption is the same as for Figure 2.

$\psi^2(\tau,f)^*\sigma(\tau,f)$. The cross-correlation analysis of the data and the template revealed the time-delay and Doppler residuals that produced the peak power in the cross-correlation function. These values were used to correct the nominal ephemerides used in the experiment.

Table 3 shows resolutions of the synthetic images used in our analysis. For example, we oversampled the Io data by factors of 4 in Doppler frequency and by 5 in time-delay. Figure 6(A) shows Ganymede's echo from 2015 January oversampled to have 5 Hz × 7 μs resolution. Figure 6(B) shows the synthetic echo that was shifted in delay and Doppler with Matlab 2D cross-correlation function xcorr2 to create a map that appears in Figure 6(C). The time-delay and Doppler

position of the peak cross-correlation was used as a correction to the predicted ephemerides (Table 1). We tested the cross-correlation method for different selections of oversampling factors in the construction of the synthetic echoes, but the resulting residuals showed no significant changes.

Harmon et al. (1994) estimated formal errors in the time-delay and Doppler frequency residuals by running Monte Carlo simulations. They stated that the "dominant source of error is random estimation error associated with the system noise." The procedure consisted of generating 50 synthetic echoes with known delay and Doppler offset that have S/Ns comparable to the observations. Gaussian white noise was added to a model echo and the standard cross-correlation analysis followed. The resulting

Figure 4. Collage of, from left to right, delay-Doppler SC radar images, fits, and the *Shape* software plane-of-sky renderings of the shape model for Ganymede (Table 2). Plane-of-sky view is contained in a 6300.0 × 6300.0 km square with 6301 × 6301 pixels. The rest of the caption is the same as for Figure 2.

formal errors were at the subpixel level. The baud used in Harmon et al. (1994) experiment was 100 μs, and their estimated 3σ delay errors were 21 and 48 μs for the two Ganymede echoes and were 87 and 90 μs for the two Callisto echoes. The Ganymede errors were different because the two echoes had different S/Ns.

We used the same procedure and likewise, obtained formal errors several times finer than the data resolution. The cross-correlation function consistently recovered correct ranges and Dopplers even for the echoes with weak S/Ns (e.g., Io). However, these errors do not include systematic uncertainties due to the unmeasured time delays in the matched filters in the data acquisition path: for the older data, obtained in 1999 and 2000, the filters were not calibrated to better than one baud in interval time-delay, and the filters that were used are no longer available for testing and calibration. Thus, we adopted the uncertainties of one-half a baud to a one full baud.

We also estimated residuals with two additional methods. The most straightforward method is a visual estimate of the center of the leading edge. We detect a point in time-delay where the neighboring pixels first cross S/Ns 2σ above the noise level. We also visually determine the center of the curvature for the first few rows of the echo and measure its offset from zero in Doppler frequency.

Residuals were futhermore estimated with the *Shape* software (Hudson 1993; Magri et al. 2007). *Shape* uses a weighted least-squares algorithm to reconstruct shapes and spin states of objects observed by radar (Hudson & Ostro 1995; Magri et al. 2007; Brozović et al. 2011; Marshall et al. 2017). We used *Shape* to generate synthetic radar echoes of the satellites based on their physical properties in Table 2. *Shape* aligned the fits and the data by optimizing the coefficients of the delay correction polynomial in an iterative χ^2 procedure. The delay correction polynomial has the form $b_1(t-t_0)+b_0$, where the coefficient b_1 has units of μs day^{-1}

and b_0 has units of μs. Here, t is the mid-time of the receiving interval on each observing day and t_0 is an arbitrary starting epoch. The time-delay correction, residual, to the ephemerides corresponds to $\mathrm{del_{corr}} = b_0$ and the Doppler frequency correction corresponds to $\mathrm{Dop_{corr}} = -b_1 Tx[\mathrm{MHz}]/[86,400\,\mathrm{s\,day}^{-1}]$, where Tx is the transmit frequency (2380 MHz for Arecibo).

3. Results

Each of the three methods described in Section 2.3 produced consistent results (Table 4). The residuals obtained with the cross-correlation method were adopted as nominal and used to produce the absolute measurements of the time delays and Doppler frequencies of the subradar points. The most precise time-delay measurements have an uncertainty of 10 μs (1.5 km). There are four of them: one for Europa, two for Ganymede, and one for Callisto. The remaining measurements have larger uncertainties, up to 250 μs (37.5 km).

We detected Io with delay-Doppler imaging setup for the first time in 2015 (Figure 2). We assigned the ranging uncertainty to be equal to the time-delay pixel resolution, 35 μs (5.25 km), which is one-half of the baud used in the observations. This uncertainty not only accounts for the methods described in Section 2.3, but is also sufficiently large to encompass the average topography on Io. Table 1 shows that the first two subradar points are relatively close to the longitudes and latitudes of >8.5 km high Hiíaka Montes North (82°.3, −1°.9), 7 km high Boösaule Montes East (263°.5, −1°.7), and 8.5 km high Boösaule Montes North (268°.8, −2°.5) (Schenk et al. 2001). If we assume that we can approximate the addition to Io's radar line-of-sight radius as $(r_0+h)\cos\alpha - r_0$, where r_0 is Io's intermediate b-axis from Table 2, h is the height of a mountain, and α is the angle between the subradar
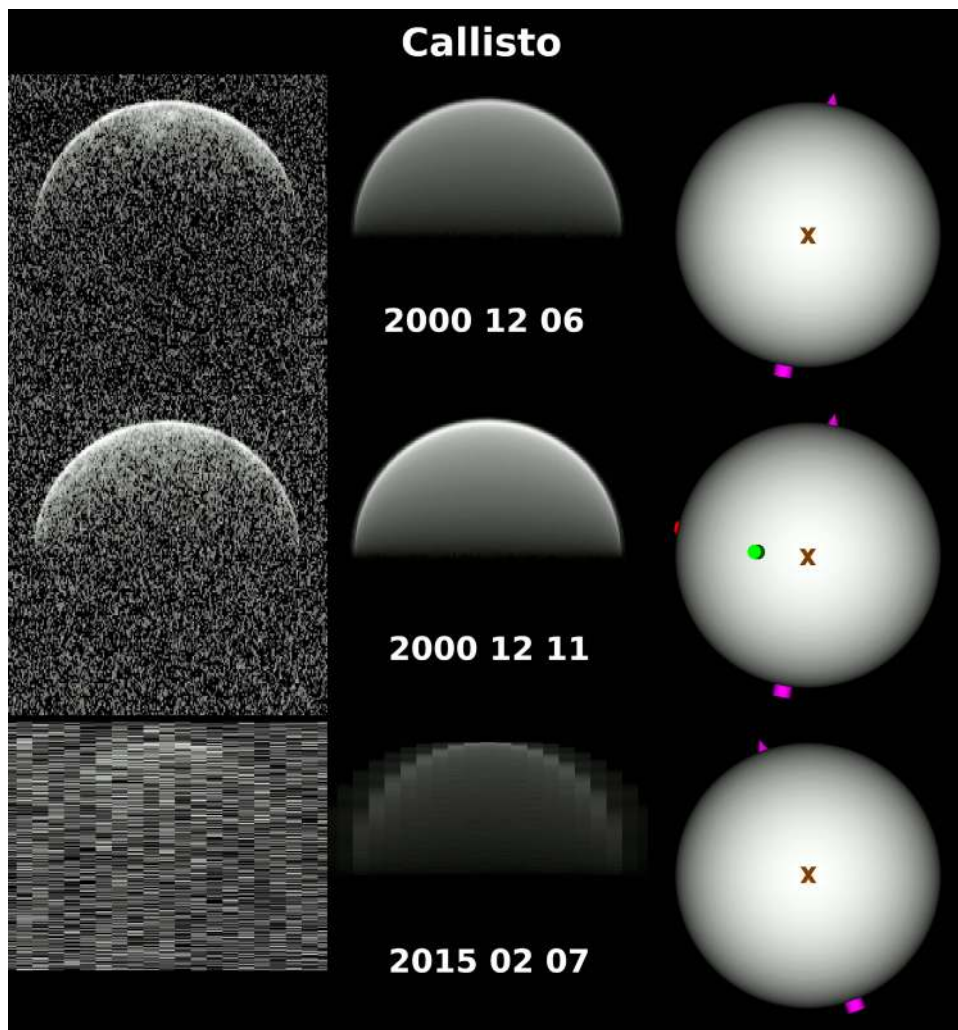
Figure 5. Collage of, from left to right, delay-Doppler SC radar images, fits, and the *Shape* software plane-of-sky renderings of the shape model for Callisto (Table 2). Plane-of-sky view is contained in a 5800.0 × 5800.0 km square with 5801 × 5801 pixels. The rest of the caption is the same as for Figure 2.

point and the mountain, then we get at most a ∼3 km addition due to the local topography. This is within ∼0.6σ of the time-delay measurement error meaning that we did not need to inflate the uncertainties any further.

Note that Table 4 shows the leading-edge residuals with respect to different ephemerides that were used at the time of observations. The planetary ephemeris was used to calculate the position of Jupiter with respect to Earth, while the satellite ephemeris determined the positions of the Galileans with respect to Jupiter. Leading-edge range predicts depend on the assumed size and orientation of the satellite. Once we calculated the absolute measurements, we were able to estimate their residuals with respect to a common combination of the planetary and satellite ephemerides and sizes (Table 5). We used the sizes and the orientations of the Galilean moons from Table 2 to calculate the distances from the center-of-mass to the subradar point. We list these in Table 5 so that the center-of-mass predicts can be retrieved.

Table 5 shows residuals with respect to the Galilean satellite ephemeris JUP310 (R. Jacobson 2020, personal communication) and the most recent planetary ephemeris DE438 (Folkner 2018). JUP310 is available from the JPL Horizons on-line solar system data and ephemeris computation service at https://ssd.jpl.nasa.gov/horizons.cgi (Giorgini et al. 1996).

We also list the residuals with respect to the Institut de Mécanique Céleste et de Calcul des Éphémérides NOE-5-2010-GAL-a satellite ephemeris (Lainey et al. 2009) and DE438. Neither of these two orbital solutions used any of the radar astrometry. Both of them are pre(radar) fit. We calculated radar observables according to the procedure outlined in Yeomans et al. (1992).

Overall, all but two time-delay residuals in Table 5 fit within their reported 3σ measurement uncertainties with respect to JUP310. However, 12 time-delay residuals, spread among all four satellites, fall outside the 3σ range for NOE-5-2010-GAL-a. The rms of the residuals in time-delay with respect to JUP310 and DE438 are 29 μs for Io, 21 μs for Europa, 58 μs for Ganymede, and 275 μs for Callisto. The rms of the residuals in time-delay with respect to NOE-5-2010-GAL-a and DE438 are 80 μs for Io, 304 μs for Europa, 380 μs for Ganymede, and 356 μs for Callisto. All but two NOE-5-2010-GAL-a Doppler residuals in Table 5 fit within their 3σ measurement uncertainties. It is likely that the measurement precision is too coarse to provide useful correction to the line-of-sight velocity. We prioritized high-resolution ranging measurements which meant that we used very coarse Doppler resolution in order to boost the S/Ns of the leading edge. Doppler frequency measurements with 10–20 Hz uncertainty in *S*-band correspond
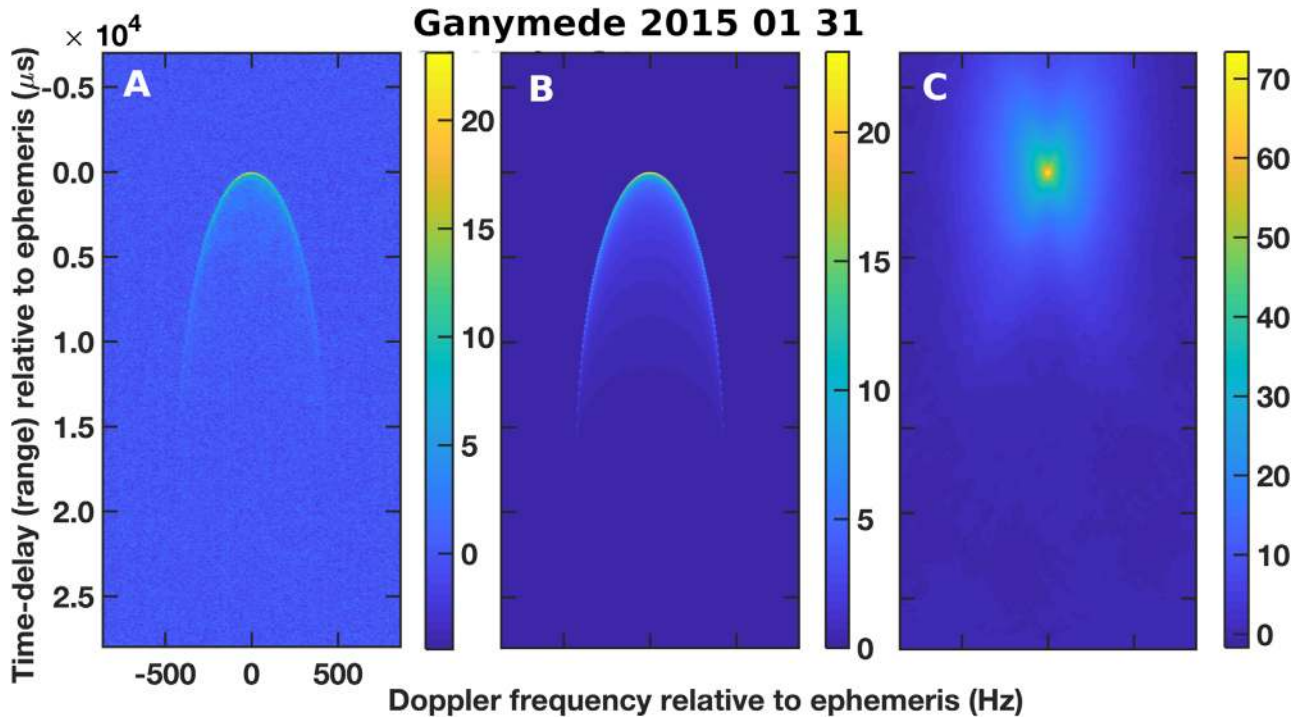
Figure 6. (A) Delay-Doppler SC image of Ganymede on 2015 January 31. The color bar shows the S/Ns in units of standard deviations above the noise level. (B) The synthetic echo of Ganymede constructed based on Equations (1) and (2). (C). Cross-correlation map of the real and the synthetic echoes obtained with Matlab function xcorr2. The brightest peak corresponds to the shift of 28 μs in delay and no shift in Doppler (Table 4) with respect to the ephemerides used in the experiment (Table 1).

Table 3
Delay-Doppler Images from 1999 to 2016

Object	Mid-time of obs. (UTC)	Image res.		Image size		FFTs	eph_row	eph_col	Synthetic echo	
		(μs)	(Hz)	rows	col.				(μs)	(Hz)
Io	2015 Feb 12 04:50:23	35	40.82	600	200	350	200.59	113.25	7	10.20
Io	2015 Feb 13 04:45:58	35	40.82	600	200	350	200.58	113.25	7	10.20
Io	2015 Feb 14 04:41:28	35	40.82	600	200	350	200.57	113.25	7	10.20
Europa	1999 Nov 8 03:34:22	50	10.00	400	250	1000	40.59	126.00	10	5.00
Europa	2015 Feb 8 05:07:37	5	20.00	4000	126	5000	502.93	89.00	5	5.00
Europa	2016 Jan 19 08:50:38	35	20.01	2000	250	714	200.58	150.99	7	5.00
Europa	2016 Jan 31 08:00:39	5	20.00	4000	250	5000	803.00	151.00	5	5.00
Ganymede	1999 Oct 30 04:28:10	20	10.00	1600	250	2500	201.56	176.00	5	5.00
Ganymede	1999 Nov 3 03:53:41	50	10.00	800	250	1000	202.34	176.00	10	5.00
Ganymede	1999 Nov 6 03:41:52	50	10.00	800	250	1000	202.50	176.00	10	5.00
Ganymede	2015 Jan 31 05:52:19	35	9.99	1000	400	1430	200.58	251.05	7	5.00
Ganymede	2015 Feb 1 05:39:11	5	10.00	6000	250	10000	402.97	176.00	5	5.00
Ganymede	2016 Jan 18 08:55:12	35	20.00	2000	250	714	500.58	150.99	7	5.00
Ganymede	2016 Jan 22 08:38:28	20	35.01	2400	250	714	400.64	140.28	5	7.00
Ganymede	2016 Feb 1 07:56:35	5	20.00	6000	250	5000	1002.99	151.00	5	5.00
Callisto	2000 Dec 6 04:28:59	250	1.95	400	1024	1024	21.19	615.40	50	1.95
Callisto	2000 Dec 11 03:36:25	250	1.95	400	1024	1024	102.04	615.40	50	1.95
Callisto	2015 Feb 7 05:25:28	5	20.00	6000	126	5000	502.98	89.00	5	5.00

Note. Listed are the midtimes of observations, the data resolution in time-delay (μs) and Doppler frequency (Hz), the number of rows and columns, the length of the Fast Fourier Transforms (FFT) used in the data processing, the row and the column of the ephemerides-predicted location of the center of the leading edge, and resolutions of the synthetic radar images used in the cross-correlation analysis (Section 2.3).

to 630–1260 mm s^{-1} in radial velocity. This is at least two orders of magnitude less precise than the Doppler astrometry obtained by *Voyager* 2, which was about a few mm s^{-1}.

Residuals reflect errors in planetary ephemeris, satellite ephemeris, or both. Formal range uncertainties in the position of Jupiter are very small in DE438 (Folkner 2018), <300 m

($\sim$2 μs). Thus, our radar residuals originate from satellite ephemerides. For the leading-edge residuals, there could also be an error in the object's size, but for the Galilean satellites, the size uncertainties are small (Tables 2 and 5). The JUP310 orbital solution has significantly smaller residuals than NOE-5-2010-GAL-a. This could be because the JUP310 ephemeris

Table 4
Position of the Satellite's Leading Edge in Time-delay and Doppler Frequency

| | | | Ephemeris Residuals | | | | | | Absolute Measurements | |
| | | | Visual | | *Shape* | | **Cross-Corr.** | | | |
Num.	Object	Mid-time of obs. (UTC)	Del. (μs)	Dopp. (Hz)	Del. (μs)	Dopp. (Hz)	**Del. (μs)**	**Dopp. (Hz)**	Time-delay $\pm 1\sigma$ (μs)	Doppler freq. $\pm 1\sigma$ (Hz)
1	Io	2015 Feb 12 04:50	49.4	−10.2	44.1	−1.4	**35.0**	**−10.2**	4343541814.4 ± 35.0	218996.0 ± 20.0
2	Io	2015 Feb 13 04:46	84.6	−10.2	95.4	5.3	**84.0**	**0.0**	4345524763.5 ± 35.0	−328541.6 ± 20.0
3	Io	2015 Feb 14 04:41	15.2	30.6	24.9	3.2	**7.0**	**10.2**	4345693639.5 ± 35.0	160766.8 ± 20.0
4	Europa	1999 Nov 8 03:34	2120.0	0.0	2114.8	27.2	**2100.0**	**25.0**	3998093174.3 ± 50.0	67845.9 ± 10.0
5	Europa	2015 Feb 8 05:08	0.4	0.0	−1.3	0.3	**−10.0**	**0.0**	4336354276.4 ± 10.0	−219136.6 ± 10.0
6	Europa	2016 Jan 19 08:51	14.7	0.2	25.7	0.4	**7.0**	**0.0**	4778150186.0 ± 35.0	144797.1 ± 10.0
7	Europa	2016 Jan 31 08:01	10.2	0.0	−12.0	−0.8	**−25.0**	**0.0**	4638002553.7 ± 20.0	475545.5 ± 10.0
8	Ganymede[h]	1992 Feb 20 05:57	⋯	⋯	⋯	⋯	⋯	⋯	4413296899.0 ± 50.0	−89175.0 ± 3.0
9	Ganymede[h]	1992 Mar 9 04:37	⋯	⋯	⋯	⋯	⋯	⋯	4417270238.0 ± 20.0	91822.1 ± 1.5
10	Ganymede	1999 Oct 30 04:28	1128.0	10.0	1147.0	3.3	**1135.0**	**5.0**	3960609284.7 ± 20.0	−220005.0 ± 10.0
11	Ganymede	1999 Nov 3 03:54	632.9	−10.0	663.9	−3.1	**650.0**	**−5.0**	3976030265.7 ± 50.0	74883.2 ± 10.0
12	Ganymede	1999 Nov 6 03:42	1125.1	0.0	1142.0	5.4	**1130.0**	**5.0**	3983261039.5 ± 50.0	−264878.5 ± 10.0
13	Ganymede	2015 Jan 31 05:52	14.7	−0.5	41.6	−0.6	**28.0**	**0.0**	4346103155.2 ± 35.0	212000.2 ± 10.0
14	Ganymede	2015 Feb 1 05:39	10.2	0.0	9.2	0.4	**−5.0**	**0.0**	4338330207.7 ± 10.0	198560.2 ± 10.0
15	Ganymede	2016 Jan 18 08:55	49.9	0.2	39.0	1.6	**21.0**	**0.0**	4787733099.7 ± 35.0	523634.5 ± 10.0
16	Ganymede	2016 Jan 22 08:38	−52.8	−9.8	−42.5	0.3	**−65.0**	**0.0**	4744013679.3 ± 20.0	214165.0 ± 10.0
17	Ganymede	2016 Feb 1 07:57	20.0	0.0	17.7	0.6	**5.0**	**0.0**	4624607414.5 ± 10.0	458722.6 ± 10.0
18	Callisto[h]	1992 Mar 3 05:05	⋯	⋯	⋯	⋯	⋯	⋯	4394993673.0 ± 90.0	59034.5 ± 2.4
19	Callisto[h]	1992 Mar 7 04:46	⋯	⋯	⋯	⋯	⋯	⋯	4402260207.0 ± 90.0	−156844.5 ± 2.4
20	Callisto	2000 Dec 6 04:29	4362.9	14.8	4462.3	19.2	**4450.0**	**19.5**	4045818071.6 ± 250.0	−553.2 ± 10.0
21	Callisto	2000 Dec 11 03:36	990.3	3.0	1040.6	5.1	**1000.0**	**5.9**	4069588213.4 ± 250.0	−246329.8 ± 10.0
22	Callisto	2015 Feb 7 05:25	−69.9	0.0	−65.6	−0.1	**−70.0**	**0.0**	4331232769.2 ± 10.0	104205.1 ± 10.0

Note. Entries report the time-delay and Doppler frequency corrections to the original ephemeris used in observations (Table 1). The first column lists the observation numbers to which we refer to in Figure 1. The ephemeris corrections (residuals) were estimated visually, with the *Shape* software, and with the Harmon et al. (1994) cross-correlation method. We adopted the last set of values (marked in bold) to obtain absolute measurements of the position of the leading edge in time-delay and Doppler frequency. Time-delay uncertainty of 10 μs is equivalent to 1.5 km, and 1 Hz uncertainty in Doppler frequency corresponds to ~63 mm s^{-1} in radial velocity at the 2380 MHz Arecibo S-band transmitter reference frequency. We include the data points from Harmon et al. (1994), marked with the letter *h*, for completeness.

was fit to a larger data set, including *Galileo* spacecraft astrometry from 1995 to 2001, and NOE-5-2010-GAL-a only included ground-based observations.

4. Discussion

4.1. Other Sources of High-precision Astrometry

Saquet et al. (2018) observed mutual events from 2014 to 2015 and reported a measurement uncertainty of ~24 mas. The rms of the residuals in the plane-of-sky coordinates was 65.5 mas with respect to JPL's JUP310 and planetary ephemeris DE430 (Folkner et al. 2014). Saquet et al. measurements are orthogonal with respect to our radar ranging measurements, and their relatively large residuals are not at odds with the small radar residuals in Table 5. Any errors in the pole of Jupiter and/or inclinations of the orbital planes of the satellites would result in larger than expected plane-of-sky residuals.

Astrometry of the Galilean satellites was also reported in Morgado et al. (2019a, 2019b). Morgado et al. (2019a) measured instants of apparent encounters of satellites in the plane of sky from 2016 to 2018. This method consists of tracking the apparent distance between two satellites on the plane of sky and identifying the time when minimum distance occurs. This type of measurement, described in Morgado et al. (2016), is not tied to the geometry of mutual events and is supposed to achieve precisions better than 30 mas (90 km).

Morgado et al. (2019a) reported 14.4 mas as the rms of the residuals with respect to JUP310 and planetary ephemeris DE435 (Folkner 2016). Additionally, Morgado et al. (2019b) reported a very precise measurement of Europa's position, with an uncertainty of 0.8 mas, based on the first stellar occultation. The offsets with respect to JUP310 ephemeris and planetary ephemeris DE438 (Folkner 2018) were −7.94 mas for $\Delta\alpha \cos \delta$ and −10.91 mas for $\Delta\delta$. These measurements are complementary to the radar observations and suggest that JUP310 may need improvement in orbital inclinations.

4.2. Future Radar Observations

The next opportunity to observe the Galilean satellites from Arecibo starts in the second part of 2022 and lasts until mid-2028. Observations will not be continuous because the rise-set times for Jupiter will sometimes be shorter than the one full RTT. This is the time needed for transmission of a radar signal. However, observations will be possible as long as there are ~15 minutes available to receive the echo past one full RTT and assuming that Jupiter is not close to the conjunction. The upcoming apparitions will be an excellent opportunity to obtain more astrometry and to improve the orbits in time for NASA's Europa Clipper and ESA's *JUICE* spacecraft arrival at Jupiter in late the 2020s or early 2030s.

The oppositions in 2023, 2024, and 2025 will be very favorable with respect to Jupiter's distance from Earth and the time that the planet spends in Arecibo's decl. window. Table 2 lists representative Arecibo S/Ns. We note that the Goldstone

Table 5
Residuals for JUP310 and NOE-5-2010-GAL-a Satellite Ephemerides

Num.	Object	Mid-time of obs. (UTC)	CTRF (km)	CTRF-1σ (km (μs))	Measurement-1σ		JUP310+DE438		NOE-5-2010-GAL-a+ DE438	
					Time-delay (μs)	Dopp. (Hz)	Resid. Del. (μs)	Resid. Dopp. (Hz)	Resid. Del. (μs)	Resid. Dopp. (Hz)
1	Io	2015 Feb 12 04:50:00	1819.8	0.3 (2)	35.0	20.0	−26.1	−10.2	−75.1	−5.1
2	Io	2015 Feb 13 04:46:00	1819.8	0.3 (2)	35.0	20.0	22.4	0.0	44.2	4.5
3	Io	2015 Feb 14 04:41:00	1822.6	0.3 (2)	35.0	20.0	−36.3	10.2	**−106.7**	8.6
4	Europa	1999 Nov 8 03:34:00	1560.5	0.3 (2)	50.0	10.0	21.9	−3.8	**587.7**	−9.3
5	Europa	2015 Feb 8 05:08:00	1560.6	0.3 (2)	10.0	10.0	−19.8	0.1	**101.0**	−4.5
6	Europa	2016 Jan 19 08:51:00	1560.4	0.3 (2)	35.0	10.0	1.0	0.0	**106.5**	−0.4
7	Europa	2016 Jan 31 08:01:00	1561.0	0.3 (2)	20.0	10.0	−29.2	0.0	−43.0	−1.1
8	Ganymede[h]	1992 Feb 20 05:57:00[b]	2631.2	1.7 (11)	50.0	3.0	20.0	−3.0	**−792.6**	−5.1
9	Ganymede[h]	1992 Mar 9 04:37:00[b]	2631.2	1.7 (11)	20.0	1.5	**−107.1**	0.1	**147.4**	4.5
10	Ganymede	1999 Oct 30 04:28:00	2631.2	1.7 (11)	20.0	10.0	−11.1	1.5	**−246.4**	7.4
11	Ganymede	1999 Nov 3 03:54:00	2631.2	1.7 (11)	50.0	10.0	4.2	−2.2	**562.6**	0.3
12	Ganymede	1999 Nov 6 03:42:00	2631.2	1.7 (11)	50.0	10.0	−128.8	−0.5	**−181.0**	5.6
13	Ganymede	2015 Jan 31 05:52:00	2631.2	1.7 (11)	35.0	10.0	34.0	0.0	119.6	1.1
14	Ganymede	2015 Feb 1 05:39:00	2631.2	1.7 (11)	10.0	10.0	0.7	0.0	1.1	2.5
15	Ganymede	2016 Jan 18 08:55:00	2631.2	1.7 (11)	35.0	10.0	29.8	0.0	56.7	0.9
16	Ganymede	2016 Jan 22 08:38:00	2631.2	1.7 (11)	20.0	10.0	−57.0	0.0	**−604.1**	−9.9
17	Ganymede	2016 Feb 1 07:57:00	2631.2	1.7 (11)	10.0	10.0	11.7	0.0	29.5	0.6
18	Callisto[h]	1992 Mar 3 05:05:00[b]	2410.3	1.5 (10)	90.0	2.4	−22.2	1.1	175.5	**8.6**
19	Callisto[h]	1992 Mar 7 04:46:00[b]	2410.3	1.5 (10)	90.0	2.4	−91.8	1.5	**−600.7**	**−9.3**
20	Callisto	2000 Dec 6 04:29:00	2410.3	1.5 (10)	250.0	10.0	416.9	0.1	476.8	2.2
21	Callisto	2000 Dec 11 03:36:00	2410.3	1.5 (10)	250.0	10.0	436.7	0.8	−107.7	3.9
22	Callisto	2015 Feb 7 05:25:00	2410.3	1.5 (10)	10.0	10.0	**−65.7**	0.0	**46.3**	0.5

Note. List of all reported radar observations of the Galilean moons from 1992 to 2016 and their residuals with respect to the latest satellite and planetary ephemerides. The first column lists the observation numbers to which we refer in Figure 1. Ephemeris is always calculated for the center-of-mass of an object. Time-delay residuals refer to the position of the leading edge. The leading edges were calculated by adding a distance from the center-of-mass to the radar reflection point (CTRF) to the ephemerides. The CTRFs implement an orientation of the three-axial ellipsoid (Table 2). We list the CTRFs used in this calculation as well as the associated CTRF uncertainties based on Table 2. The measurements marked with the letter *h* are Harmon et al. (1994) time delays and Dopplers, which we include for completeness. We inflated Harmon et al. measurement uncertainties by a factor of three because their original weights appeared too optimistic given the data resolution and the S/Ns. Residuals marked in bold exceed their 3σ measurement uncertainties.

Solar System Radar in California can observe the satellites every year at opposition, but the S/Ns are ∼15 times (Naidu et al. 2016) lower than at Arecibo. Receiving Goldstone transmissions with the Green Bank 100 m diameter antenna in West Virginia increases the S/Ns by a factor of ∼2 (Naidu et al. 2016), but this is still significantly weaker than the S/Ns at Arecibo. Furthermore, bistatic observations introduce ambiguity into time-delay measurements that need to be calibrated with respect to objects with well-known orbits, such as Venus or Mars.

The 2022–2028 observing window at Arecibo may also be a good opportunity to attempt to detect Jupiter's moon Amalthea. Amalthea is 250 × 146 × 128 km (Thomas et al. 1998a) in size, and it is the third closest satellite of Jupiter. Its small size and proximity to Jupiter make it a difficult observing target for optical telescopes. We estimate that the S/Ns at Arecibo are ∼3 per day, assuming a 900 kW transmit power and a radar albedo of 0.3. Our S/N estimates do not account for Jupiter being a strong *S*-band radio source which could significantly impact the echo strength. It is possible that some of the noise can be reduced if we use a slight pointing offset while still keeping Amalthea in the Arecibo's 120″ wide beam (3 dB). Anderson et al. (2005) suggested that Amalthea is a low-density object, likely composed of water ice and some rock, so its radar albedo (and S/Ns) could be several times higher, facilitating its detection. The radar scattering properties of Amalthea would help determine its composition and a range detection with 500 μs (75 km) precision would help to improve its orbit.

5. Conclusions

Radar observations provide very precise measurements of the line-of-sight positions for the Galilean satellites. We obtained 18 ranging measurements from 1999 to 2016 among which are the first delay-Doppler detections of Europa in 1999 and Io in 2015. The highest precision measurements of Europa, Ganymede, and Callisto have uncertainties of only 1.5 km and can be compared to the precision of spacecraft astrometry or stellar occultations. Our measurements of Io with 5.25 km uncertainty are the most precise ground-based measurements of this object to date.

The rms of the normalized residuals are 0.82 for Io, 1.25 for Europa, 2.17 for Ganymede, and 3.17 for Callisto for JUP310 and DE438. Alternatively, NOE-5-2010-GAL-a and DE438 have rms of 2.27, 7.97, 12.38, and 3.84 for the four satellites. The rms of the normalized residuals should be below three and preferably closer to one for an acceptable fit quality. We thus conclude that NOE-5-2010-GAL-a would benefit from updates of orbits of Ganymede, Europa, and Callisto while JUP310 would benefit from an updated orbit of Callisto.

ORCID iDs

Robert A. Jacobson ⓘ https://orcid.org/0000-0002-8844-724X
Shantanu P. Naidu ⓘ https://orcid.org/0000-0003-4439-7014

References

Anderson, J. D., Jacobson, R. A., Lau, E. L., et al. 2001a, BAAS, 33, 1101
Anderson, J. D., Jacobson, R. A., McElrath, T. P., et al. 2001b, Icar, 153, 157
Anderson, J. D., Johnson, T. V., Schubert, G., et al. 2005, Sci, 308, 1291
Archinal, B. A., Acton, C. H., A'Hearn, M. F., et al. 2018, CeMDA, 130, 22
Black, G. J. 2002, in ASP Conf. Ser. 278, Single-Dish Radio Astronomy: Techniques and Applications, ed. S. Stanimirović et al. (San Francisco, CA: ASP), 271
Black, G. J., Campbell, D. B., & Nicholson, P. D. 2001, Icar, 151, 167
Brozović, M., Benner, L. A. M., Nolan, M. C., et al. 2011, Icar, 216, 241
Campbell, D. B., Chandler, J. F., Ostro, S. J., et al. 1978, Icar, 34, 254
Campbell, D. B., Chandler, J. F., Pettengill, G. H., & Shapiro, I. I. 1977, Sci, 196, 650
Campbell, J. K., Synnott, S. P., & Bierman, G. 1983, ITAC, 28, 256
Folkner, W. M. 2016, Planetary Ephemerides DE435, Inter Office Memorandum 392R-16-003, ftp://ssd.jpl.nasa.gov/pub/eph/planets/ioms/de435.iom.pdf
Folkner, W. M. 2018, Planetary Ephemerides DE438, Inter Office Memorandum 392R-18-004, ftp://ssd.jpl.nasa.gov/pub/eph/planets/ioms/de438.iom.pdf
Folkner, W. M., Williams, J. G., Boggs, D. H., et al. 2014, IPNPR, 196, 1 ftp://naif.jpl.nasa.gov/pub/naif/generic_kernels/spk/planets/de430_and_de431.pdf
Giorgini, J. D., Yeomans, D. K., Chamberlin, A. B., et al. 1996, BAAS, 28, 1158
Gomes-Júnior, A. R., Assafin, M., Beauvalet, L., et al. 2016, MNRAS, 462, 1351
Harcke, L. J., Zebker, H. A., Jurgens, R. F., et al. 2001, LPI, 32, 1369
Harmon, J. K. 2002, ITGRS, 40, 1904
Harmon, J. K., Ostro, S. J., Chandler, J. F., et al. 1994, AJ, 107, 1175
Hudson, R. S., & Ostro, S. J. 1995, Sci, 270, 84
Hudson, S. 1993, RemS, 8, 195
Jacobson, R. A., Haw, R. J., McElrath, T. P., et al. 2000, JAnSc, 48, 495
Lainey, V. 2016, CeMDA, 126, 145
Lainey, V., Arlot, J.-E., Karatekin, O., et al. 2009, Nat, 459, 957
Lieske, J. H. 1978, A&A, 65, 83
Lieske, J. H. 1980, A&A, 82, 340
Lieske, J. H. 1986a, A&A, 154, 61
Lieske, J. H. 1986b, A&AS, 63, 143
Lieske, J. H. 1998, A&AS, 129, 205
Magri, C., Ostro, S. J., Scheeres, D. J., et al. 2007, Icar, 186, 152
Marshall, S. E., Howell, E. S., Magri, C., et al. 2017, Icar, 292, 22
Morgado, B., Assafin, M., Vieira-Martins, R., et al. 2016, MNRAS, 460, 4086
Morgado, B., Assafin, M., Vieira-Martins, R., et al. 2019a, MNRAS, 482, 5190
Morgado, B., Benedetti-Rossi, G., Gomes-Júnior, A. R., et al. 2019b, A&A, 626, L4
Naidu, S. P., Benner, L. A. M., Margot, J.-L., et al. 2016, AJ, 152, 99
Nimmo, F., Thomas, P. C., Pappalardo, R. T., et al. 2007, Icar, 191, 183
Ostro, S. J. 1993, RvMP, 65, 1235
Ostro, S. J., Campbell, D. B., Simpson, R. A., et al. 1992, JGR, 97, 18277
Sampson, R. A. 1921, MmRAS, 63, 1
Saquet, E., Emelyanov, N., Robert, V., et al. 2018, MNRAS, 474, 4730
Schenk, P., Hargit, H., Wilson, R., et al. 2001, JGR, 106, 201
Stone, R. C. 2000, AJ, 120, 2124
Stone, R. C. 2001, AJ, 122, 2723
Stone, R. C., & Harris, F. H. 2000, AJ, 119, 1985
Sulzer, M. P. 1986, RaSc, 21, 1033
Thomas, P. C., Burns, J. A., Rossier, L., et al. 1998a, Icar, 135, 360
Thomas, P. C., Davies, M. E., Colvin, T. R., et al. 1998b, Icar, 135, 175
Yeomans, D. K., Chodas, P. W., Keesey, M. S., et al. 1992, AJ, 103, 303